A fluid dynamic gauging device for measuring fouling deposit thickness in opaque liquids at higher temperature and pressure

A. Ali, G.J. Chapman, Y.M.J. Chew[†], T. Gu, W.R. Paterson & D.I. Wilson
Department of Chemical Engineering & Biotechnology, New Museums Site, Pembroke Street, Cambridge, CB2 3RA, UK
[†]Department of Chemical Engineering, University of Bath, Claverton Down, Bath, BA2 7AY, UK

Abstract

We report proof-of-concept results for a fluid dynamic gauging (FDG) device for measuring the thickness and strength of soft solid fouling layers immersed in an opaque liquid *in situ* and in real time at elevated pressures and temperatures. The device reported here is configured to make measurements on the inner rod of an annular flow test section but the concept is generic. Data are presented from tests using mineral oil at temperatures and pressures up to 140 °C and 10 bara, respectively. Problems with the prototype hardware prevented testing up to the design limits of 270 ºC and 30 bara. The practical working range of the gauge, *i.e.* $0.10 < h/d_t < 0.25$, proved to be unaffected by the pressure and temperature. h is the nozzle-surface clearance and d_t the nozzle throat diameter. At smaller h/d_t values the pressure drop across the nozzle is very high and this can serve as an alarm for close approach. The range of discharge coefficient, $C_{d,}$ values obtained is sensitive to flow rate when the Reynolds number at the throat, Re_t, falls below 20. A useful range of C_d values is obtained when $Re_t > 40$. Computational fluid dynamics (CFD) simulations of the gauging flow in these quasi-static experiments (no bulk liquid flow) gave good agreement with experimental data for the cases tested. The CFD results showed that the low Re_t regime is related to creeping flow in the nozzle. CFD calculations of the shear stress being imposed on the surface being gauged gave good agreement with an analytical model for flow between parallel discs, indicating that the latter can be used to estimate the maximum shear stress imposed by the gauging flows measurements.

Keywords: *CFD, fouling, fluid dynamic gauging, measurement, surface*

Nomenclature

Latin

C_d	discharge coefficient	-
C_d^{∞}	discharge coefficient, asymptotic value	-
C_f	Fanning friction factor	-
d	tube diameter	m
d_t	nozzle throat diameter	m
E_a	activation energy	J mol^{-1}
f	friction factor	-
g	acceleration due to gravity	m s^{-2}
h	clearance between nozzle and deposit layer	m
h_i	elevation at station i	m
h_0	clearance between nozzle and substrate	m
l'	reduced gauging nozzle length	m
L	length of test section	m
L_{arm}	LVDT armature length	m
L_{eff}	effective length between stations (1) and (2)	m
L_{LVDT}	LVDT body length	m
L_{nozzle}	gauging nozzle length	m
$\dot{m}$	discharge mass flow rate	g s^{-1}
$\dot{m}_{ideal}$	ideal discharge mass flow rate	g s^{-1}
Ne	number of mesh elements	-
P	system pressure	bara
P_i	pressure at station i	Pa
ΔP_{12}	pressure drop across the gauging nozzle	bar
Re	Reynolds number	-
Re_t	Reynolds number at the throat of the gauging nozzle	-
r	radial co-ordinate of gauging nozzle	m
r_i	gauging tube inner radius	m
r_{inner}	inner rod diameter	m
s	lip width	m
T	temperature	°C
U	bulk velocity	m s^{-1}
u	x-wise velocity	m s^{-1}
v	y-wise velocity	m s^{-1}
v_i	velocity at station i	m s^{-1}
v_{max}	maximum y-wise velocity	m s^{-1}
$\bar{v}$	average velocity	m s^{-1}
w	z-wise velocity	m s^{-1}
x	co-ordinate	-
y	co-ordinate	-
z	co-ordinate	-

Greek

δ	thickness of fouling layer	m
λ	nozzle entry length	m
μ	fluid viscosity	Pa s

μ_0	fluid viscosity at 0 K	Pa s
ρ	fluid density	kg m^{-3}
φ	nozzle angle	-
ϕ	fraction of annulus	-
τ	wall shear stress	Pa
τ_{yr}	wall shear stress on y-plane in the r-direction	Pa

CFD	computational fluid dynamics
FDG	fluid dynamic gauging
HIPOR	higher temperature and pressure operations oil rig
IAW	inner annulus wall
LVDT	linear variable displacement sensor
OAW	outer annulus wall
PTFE	polytetrafluoroethylene
SS	stainless steel

1. Introduction

The build-up of fouling deposits on heat transfer surfaces is a serious industrial problem affecting heat exchanger performance and operability. The extent of fouling is often quantified experimentally through the reduction in heat transfer performance or increase in pressure drop across units. Understanding the mechanisms involved in fouling and cleaning, which are currently poorly understood, requires careful experimentation to measure the deposit strength and thickness as well as other parameters. Fouling layers can be formed from flowing liquids and gases. Since many fouling layers formed from liquids are soft and deform readily when removed from their native liquid environment, and the liquids are usually opaque, measuring their thickness reliably under experimental conditions is a challenge.

Fluid dynamic gauging (FDG) is a non-contact measurement technique developed by Tuladhar *et al*. (2000) to measure the thickness of soft fouling layers in liquid environments in situ and in real time. The principle of FDG is illustrated in Figure 1. A nozzle is located at a distance, h_o, from a solid surface immersed in liquid. A pressure drop, ΔP_{12}, is imposed across the nozzle, causing liquid to flow into the nozzle with a mass flow rate, $\dot{m}$. The flow rate is very sensitive to the clearance, h, so that measurements of $\dot{m}$ and ΔP_{12} allow h to be calculated without making contact with the layer. The range of clearances over which useful measurements can be made is $h/d_t < 0.25$ where d_t is the inner diameter of the gauging nozzle. The thickness of the fouling layer, δ, can then be calculated by difference, *viz*.

$$\delta = h_o - h \qquad (1)$$

where h_0 is the distance from the nozzle to the underlying substrate, measured independently or when the substrate is clean.

The primary requirement for the technique is that the surface being gauged remains stiff over the duration of the test. The flow of liquid underneath the nozzle at low values of h can generate significant shear stresses on the deposit. Chew *et al*. (2004a,b) demonstrated that FDG can be used to determine the strength (or yield point) of a deposit layer. They quantified the normal and shear stresses imposed on the surface using CFD simulations for flows in the laminar and inertial regime and demonstrated that the shear stresses generated in the nozzle region were dominated by the gauging flow contribution with little influence from the bulk. It should be noted that the flow through the nozzle and past station 2 in Figure 1 is set to lie in the laminar regime.

Tuladhar *et al*. (2000) demonstrated the FDG concept with measurements on flat surfaces immersed in a stagnant bath of liquid. As a small flow of liquid is withdrawn through the gauging nozzle, this mode of operation is labelled ‘quasi-static FDG’. Tuladhar *et al*. (2003) subsequently demonstrated that

FDG deposit thickness measurements could be made on flat surfaces, in this case the wall of a square duct, whilst the bulk liquid was flowing across the surface. This mode of gauging was labelled ‘duct flow FDG’.

Gu *et al*. (2009, 2011a,b) extended the technique to make measurements on the inner, convex surface of annular geometries (*i.e.* curved surfaces), termed ‘annular flow FDG’. The flow patterns in these geometries are well understood to the extent that both heated and cooled rods are used in fouling and cleaning studies, as summarized by Gu *et al*. (2009). They demonstrated that annular flow FDG can be used to make measurements under both quasi-static conditions and where the bulk liquid is in the laminar, transitional and turbulent flow regimes. CFD simulations compared well with experimental data for quasi-static flow conditions, enabling estimation of the shear stresses exerted by gauging flows on the substrate.

Many of the FDG applications reported to date have involved liquids at temperatures near ambient (10 – 110 °C) and pressures ranging from 1 – 3 bara. Several industrial applications feature higher temperature and pressure conditions. A particularly important area is the fouling of heat exchangers used to process crude oil, where the liquid can reach 300 ºC and 30 bara. Macchietto *et al*. (2010) reported the development of an experimental fouling test rig designed to operate under these conditions. One of the test sections on their high temperature and pressure oil (HIPOR) fouling unit employed an annular flow section with a heated central rod. This paper reports the development of an FDG device for measuring deposit layer thickness in apparatuses such as the HIPOR unit where, in addition to the high temperature and pressures, the liquid is opaque and flammable. Results are presented with a mineral oil demonstrating proof of concept for quasi-stagnant operation at liquid temperatures up to 140 ºC and pressures up to 10 bara.

2. FDG measurements at elevated pressure and temperature

2.1 Pressure-mode FDG

In addition to h and ΔP_{12}, the mass flow rate is sensitive to the nozzle throat diameter, d_t, the nozzle lip width, s, the liquid density, ρ, and viscosity, μ. A dimensional analysis (see Tuladhar *et al.*, 2000) gives

$$C_d = f\left(\frac{h}{d_t}, \frac{s}{d_t}, Re_t\right) \tag{2}$$

where C_d is the discharge coefficient, which is the ratio of $\dot{m}$ to the ideal mass flow rate through the nozzle and accounts for the energy losses associated with flow around the nozzle:

$$C_d = \frac{\text{actual mass flow rate}}{\text{ideal mass flow rate}} = \frac{\dot{m}}{\frac{\pi}{4} d_t^2 \sqrt{2\rho\Delta P_{12}}} \tag{3}$$

Re_t is the Reynolds number evaluated at the throat of the nozzle diameter.

Initial variants of FDG employed 'mass-mode' operation, whereby ΔP_{12} is held constant and $\dot{m}$ measured to give h/d_t. Equations (2) and (3) shows that $\dot{m}$ is then uniquely related to h/d_t for a given nozzle shape. Mass-mode operation is ideally suited to operation at near-ambient pressure, as a hydrostatic head can cheaply supply the pressure driving force. Controlling pressure differences to small values (typically a few kPa for a 1 mm nozzle) at higher pressures is challenging, and the associated variation in flow rate of a hazardous liquid (and the risk of spillage if pressure control is lost) means that mass-mode operation is unattractive. A second reason is that Tuladhar *et al*. (2003) reported that, under certain conditions, C_d could exhibit multiple steady states in bulk-flow FDG at a given h. This occurred when $\dot{m}$ became a significant fraction of the bulk flow rate, leading to strong interaction between the bulk and gauging flows. This limited FDG measurements under such conditions, as C_d must be uniquely related to h/d_t for a given imposed ΔP_{12}. In practice, the amount of liquid to be withdrawn through the gauging nozzle will be set to be a small fraction of the total flow rate in order to avoid significant changes in the bulk flow.

Considerations such as these prompted the development of 'pressure-mode' FDG. In this case, $\dot{m}$ is set and ΔP_{12} is measured as h/d_t is varied. Inspection of equations (2) and (3) shows that C_d is proportional to $\Delta P_{12}^{-0.5}$: ΔP_{12} increases as the nozzle approaches the surface and this confers advantages in terms of the accuracy required for a differential pressure transducer as well as setting alarms to warn of close approach to the surface. Pressure-mode duct flow FDG has been demonstrated in cross-flow microfiltration (Lister *et al.* 2010; Lewis *et al*., 2012), ultrafiltration (Jones *et al*., 2012) and annular configurations (Gu *et al*., 2011a,b). Pressure-mode FDG is easier to implement at higher pressures and overcomes the problem of multiple steady states, as $\dot{m}$ can be restricted to a small

fraction of the bulk flow. The studies above employed aqueous solutions at pressures ≤ 2.6 bara and temperatures ≤ 110 ºC.

2.2 FDG probe

Figure 2 is a schematic of the high pressure FDG probe. The annulus dimensions (inner rod diameter, r_{inner}, is 24 mm and the internal diameter of the outer pipe is 35 mm) are those of the HIPOR annular fouling test rig reported by Macchietto *et al.* (2010). The nozzle design is similar to that reported by Gu e*t al*. (2009), namely d_t = 1 mm, s = 0.5 mm, λ = 1.5 mm with an internal nozzle angle, φ, of 45º. The tube internal diameter, d, was 4 mm with a wall thickness of 2 mm. The device was constructed from 316L stainless steel. All connections were fabricated using 316L SS ¼ inch Swagelok® tubing.

The tube was located in a cylindrical chamber with three mounts for high temperature PTFE spring-loaded seals (S) (DME Seals) creating two internal chambers. The first seal isolated the device from the oil in the annular test section. The space adjacent to the outer pipe was a vapour chamber that was swept continuously by nitrogen gas to remove any leaked oil (ports E-N in Figure 2). The second chamber was the receiver for the gauging flow: the tube wall in this section was drilled with many 1 mm diameter holes to allow the oil to pass through with minimal pressure drop. This chamber was filled initially by allowing oil to leave via the high port vent (G), which was otherwise sealed by a pressure relief valve. The gauging flow leaves via the exit port (H).

A stepper motor (M) and controller (Zaber Technologies, NA14B16 and T-CD-1000) manipulated the nozzle position. The mounting on the outer pipe wall contains a recess so that the nozzle can be withdrawn completely from the annular flow region. A linear variable displacement transducer (I-J) (LVDT, RDP Group, D5/300AG) recorded the position of the nozzle within the gauge independently to an accuracy of ±20 μm. The stepper motor movement fittings included a mechanical stop to prevent the nozzle contacting the inner rod surface.

The annular test section and FDG probe were heated using electric heating tape. A mechanical stopper (O) prevented the gauging nozzle from touching the inner rod. This prototype did not allow the temperature of the oil in the nozzle or flow path to be measured directly. The temperature was estimated using a K-type thermocouple (E) that measured the outer surface temperature of the nozzle, close to the outer annulus wall. The inner annulus wall, gauging tube, HIPOR FDG and outer annulus wall all expand at higher temperatures. The expansion of the first two parts brings the gauging nozzle closer to the surface, whilst the latter two move it away. The accuracy of FDG thickness measurement is around ± 10 μm (Gordon *et al*., 2010) so the effect of thermal expansion on the distance from the nozzle to the inner tube surface has to be accounted for. Separate calculations (not reported here) indicated that the nozzle position could change by 470 μm when the temperature was raised to 140 ºC.

Thermal expansion was considered in all results reported here. The time taken for the material to expand was calculated as (~ 5 s) compared to the time required to heat the oil to its test temperature (several minutes).

2.3 Test apparatus

The high pressure FDG probe was mounted on a short (approximately 30 cm long) section of annular test section in the flow loop shown in Figure 3. In the quasi-static tests reported here, mineral oil was pumped from a reservoir around the system using a gear pump (Ismatec Instruments, MVZ-01412-3A) controlled via the pump speed and a manual control valve. The flow rate was measured directly downstream of the probe using a piston flow meter (Max Machinery, model 214-410). A non-return valve was located in the line to protect the flow meter. The flow meter was calibrated separately.

The gear pump delivered a maximum system pressure of 1.1 bara so the oil circuit was pressurised by a nitrogen gas overblanket in the reservoir. The absolute system pressure was recorded using a pressure gauge. The pressure drop across the FDG probe was measured using a differential pressure transducer (SensorsONE, PD-33X) connected to tappings on the annulus and the probe exit, located at the same elevation. Data from the flow meter, thermocouple, LVDT and differential pressure transducer were collected on a PC (Athlon XP 2200+, 1 GB RAM) running LabView™ (version 8.0). This application was also used to control the stepper motor.

The test oil, Paratherm™ NF, has a density of 887 kg m^{-3} and a viscosity of 44 mPa s at ambient temperature and pressure (Paratherm™ Corporation, 2011). Its rheology was studied on a controlled stress rheometer (Bohlin Instruments, CV120) using 40 mm smooth parallel plates. The oil was Newtonian and the viscosity decreased with increasing temperature. The effect of temperature followed the Andrade relationship:

$$\mu = \mu_o \exp\left(\frac{E_a}{RT}\right) \tag{4}$$

where μ_0 is a prefactor, E_a is a pseudo-activation energy, R is the molar gas constant and T is the temperature. The parameters found for the oil were E_a = 415 J mol^{-1} and μ_0 = 13 Pa s.

2.4 Testing protocol

Calibration curves (plots of C_d versus h/d_t) were obtained by moving the gauging nozzle towards the inner rod surface, starting from some distance away (i.e. $h/d_t > 1$), in steps and recording ΔP_{12}, $\dot{m}$ and h at each step. Following this 'advancing' series, a second series of measurements was made, in retreating mode. Comparison of the two series serves to test experimental reproducibility. An interval of ~ 10 s was required for accurate measurement of $\dot{m}$ (±2 %). For these calibration measurements the stepper motor was moved manually via the LabView™ application. When measuring deposit layer

thickness, the device could be programmed to maintain a constant nozzle-surface separation, as reported by Gordon *et al.* (2010), to ensure that the shear forces exerted by the gauging flow on the fouling layer remain constant.

The pressure change across the nozzle, ΔP_{12}, cannot be measured directly. The overall pressure drop across the annular test section and gauging nozzle, $\Delta P_{\text{overall}}$, was measured using the differential pressure transducer. Frictional losses occurring across the fittings were corrected by:

$$\Delta P_{12} = \Delta P_{\text{overall}} - \Delta P_{\text{fittings}} \tag{5}$$

where $\Delta P_{\text{fittings}}$ is the pressure drop measured for similar temperatures and flow rates when there is no gauging nozzle present. $\Delta P_{\text{fittings}}$ accounted for approximately 5 – 75% of $\Delta P_{\text{overall}}$, depending on h/d_t. Under gauging conditions ($0.05 < h/d_t < 0.20$) the fraction of the total pressure drop due to friction losses was 5 – 10%. $\Delta P_{\text{fittings}}$ decreased with temperature and was independent of pressure. C_d was then calculated using equation (3).

3 CFD Simulations

Previous CFD studies of FDG flows have demonstrated that the shear stress exerted by the gauging flow on the surface can be estimated reasonably well in quasi-static and slower flows (bulk flow $Re <$ 2000). A short set of simulations of the high pressure FDG device were performed for quasi-static operation only and are presented alongside experimental results here to demonstrate that the calculations are tractable on a standard PC. It should be noted that simulation of the flow when the bulk liquid is in the turbulent regime represents a challenging task and is not attempted here. In the quasi-static experiments studied here the flow was in the laminar regime throughout the system. Under such flow conditions FDG can yield reliable thickness measurements and estimates (for qualitative comparison) of deposit strength.

3.1 Governing equations

As the liquid is Newtonian, approximately isothermal and incompressible, the steady-state Navier-Stokes and continuity equations describe the fluid dynamics:

Continuity: $$\nabla \boldsymbol{v} = 0 \tag{6}$$

Navier- Stokes $$\rho \boldsymbol{v} \cdot \nabla \boldsymbol{v} = -\nabla P + \mu \nabla^2 \boldsymbol{v} + \rho g \tag{7}$$

where $\boldsymbol{v}(r)$ is the velocity vector, P is the pressure and the viscosity, μ, is determined using equation (4). The acceleration due to gravity, g, is set to zero as its contribution is small (see Chew *et al.* 2004b).

The simulations reported here were performed using the finite element modelling package, COMSOL Multiphysics® version 4.3, employing the SPOOLES direct solver running on a PC (2.61 GHz dual core processor and 3.25 GB RAM). Solution times varied from 5 to 20 minutes to compute.

Figure 4 shows the model geometry. It exhibits a plane of symmetry and, as the bulk liquid is effectively stagnant, it is not necessary to model the entire half annulus. Cartesian co-ordinates were employed.

Boundary conditions

The liquid enters the annulus at the base and leaves through the gauging tube. The boundary conditions are those reported by Gu *et al*. (2009), namely

(*i*) Annulus inlet, $x = -L'/2$

An average inlet velocity was assumed by specifying a fixed mass inflow. The *y*-wise and *z*-wise velocities were set to zero at this boundary.

(*ii*) Gauging tube outlet, $y = -(r_{inner} + h + l')$

At the tube outlet the flow is assumed to be fully developed, *i.e*. Poiseuille flow, giving

$$v(r) = v_{max}\left(1 - \frac{r}{r_i}\right) \qquad (8)$$

where v is the velocity at radial co-ordinate, r: v_{max} is the maximum (centreline) velocity in the tube and r_i corresponds to the inner radius of the gauging tube. l' was varied by numerical trial and error to ensure that the flow at the tube outlet was fully developed.

(*iii*) Walls

The inner and outer walls of the annulus, gauging nozzle and tube, as well as the annulus top, were all treated as impermeable boundaries with no slip.

(iv) Plane of symmetry,

There was no flow across the x-y and x-z planes, giving:

$$\mathbf{n} \cdot \mathbf{v} = 0 .$$

where **n** is the normal vector.

(v) Annulus base, $z = L'/2$

The annulus base was treated as an impermeable boundary.

The average inlet velocity (boundary condition (i)) is set as the input parameter and the flow field and pressure fields are calculated. The pressure drop across the nozzle is extracted from the solution and used to calculate $C_{d,sim}$ for comparison with the C_d value obtained in experiments. Calculation tolerances, comparing the values of velocity from successive iterations, were set below 10^{-6} m/s (where typical throat velocities reached ~ 1 m s^{-1}). The flow rate at the gauging tube outlet is compared with the inlet value as a measure of convergence accuracy. Agreement in mass flow rate to better than 1% was obtained in all simulations reported here.

3.2 Meshing and convergence

The domain was modelled with tetrahedral elements. The largest velocity and pressure gradients were located in the region below the nozzle, so mesh elements were concentrated there. The effect of the number of mesh elements, N_e, on simulation accuracy is reported for a representative case in Table 1. Increasing N_e results in increased accuracy until N_e ~ 50,000, above which there is incremental improvement for greater computational effort. The results reported in subsequent tables and figures were taken from simulations with satisfactory mass balances (flow in ≈ flow out) and a difference between experimental and simulation values of 1 - 2%.

There is an upper limit to N_e set by the computer memory. A mesh of sufficient resolution in the nozzle region and the same dimensions of the actual gauging device exceeded this limit for the PC used here. Working with a reduced nozzle length, l', annulus length, L', and the fraction of the annulus, ϕ, ($\phi \leq 0.5$) was investigated systematically for the same case as in Table 1. Table 2 shows that L' could be reduced considerably from the device length without loss of accuracy. Similar results were obtained for l' and ϕ. Table 3 summarises the standard dimensions used in subsequent simulations and Figure 5 shows the refined mesh.

4. Results and Discussion

4.1 Ambient pressure and temperature

The plot of ΔP_{12} against h/d_t for fixed $\dot{m}$ at ambient conditions in Figure 6 shows that the device performs pressure-mode gauging successfully. The expected behaviour is evident (see Gu *et al.*, 2009): distant from the surface ($h/d_t > 0.25$) the pressure drop across the nozzle shows little effect of clearance, whereas for $h/d_t < 0.25$, ΔP_{12} increases noticeably with clearance. The corresponding C_d values are plotted alongside the raw data in the Figure. The $C_d - h/d_t$ profile, termed a calibration plot, shows three regions. In region A, $h/d_t < 0.1$, C_d is almost constant (here, ~ 0.05) and less sensitive to clearance. On flat substrates, C_d approaches zero as $h/d_t \rightarrow 0$ and the lower limit observed here arises from the curvature of the surface. Region A was labelled the 'curvature region' by Gu *et al*. (2009). It serves a useful purpose here as ΔP_{12} increases strongly as the nozzle approaches the surface and can

be used to trigger an alarm for close approach. In region B, $0.1 \leq h/d_t < 0.25$, C_d increases linearly with h/d_t and is the region in which FDG thickness measurements can usefully be made. In Region C, $h/d_t > 0.25$, C_d is relatively insensitive to h/d_t, and approaches a limiting value, labelled C_d^∞, asymptotically. In gauging measurements the nozzle will normally start distant from the surface and ΔP_{12} will therefore not change until it approaches the surface. At higher P, where equipment failure (e.g. leakage) is more likely to occur, comparing C_d in region for $h/d_t > 0.25$ can be used to check whether the nozzle is blocked or other parts are functioning correctly.

The calibration plot in Figure 6 exhibits the trend reported by Gu and co-workers (2011a,b) but the C_d^∞ value is noticeably smaller than the range of values in their work ($0.5 < C_d^\infty < 0.9$). Similarly low values of C_d^∞ were reported for experimental and CFD simulation studies of FDG on flat surfaces at low Re_t by Chew *et al.* (2004a). As Re_t approaches unity, viscous losses in the flow become comparable to inertial losses and the Bernoulli equation does not provide an appropriate estimate of the ideal fluid flow. C_d is then no longer an appropriate dimensionless group to characterise the flow, as this is derived from the Bernoulli equation. Chew *et al.*'s CFD simulations, supported by experiments using viscous liquids, showed that C_d becomes strongly dependent on Re_t and independent of h/d_t for $Re_t < 8$. In the creeping flow regime C_d becomes proportional to $\sqrt{Re_t}$ (see Appendix).

The effect of flow rate was investigated under ambient conditions for Re_t ranging from 0.3 to 15. The latter value is the limit set by the gear pump at this temperature and corresponds to a mass flow rate of 0.79 g s^{-1}. The profiles in Figure 7 show a marked difference in behaviour between $Re_t = 1.1$ and $Re_t = 7$ which is consistent with the work by Chew *et al.* (2004b) on flat surfaces. These results indicate that in practise is a lower limit on the working flow rate for FDG measurements, corresponding to $Re_t \sim 7$. FDG measurements remain feasible at lower flow rates, but more accurate measuring devices are required than those used here. The profiles obtained at higher temperature are discussed in section 4.3.

4. 2 Higher pressure operation

Figure 8 shows calibration plots obtained at pressures of 1, 4, 7 and 10 bara at $Re_t = 7$ and ambient temperature. C_d is independent of the absolute pressure below 10 bara. The values collected at 10 bara for $h/d_t > 0.25$ are noticeably smaller than the other data sets, which is attributed to slow leaks in the system: a leak will lower the recorded values of $\dot{m}$ and thus reduce C_d (see equation (3)). This effect is only evident at $h/d_t > 0.2$ because at small clearances the value of C_d is more sensitive to the large pressure drop across the nozzle than a small difference in flow rate.

The calibration plots in Figure 9 show that C_d is independent of the locating mode and demonstrates that the mechanical action is reliable. Similarly good agreement was observed for all ambient

temperature tests. The error bars in these data sets are significant and arise from the accuracy of the differential pressure transducer. Reduction in the measurement uncertainty will require optimisation of the operating parameters (flow rate, pressure drop) and sensor cost.

4. 3 Higher temperature and pressure operation

The effect of temperature was investigated at atmospheric pressure up to the limit of 138 °C set by the prototype's heating arrangement. Fewer data points were collected at the highest temperature owing to difficulties in temperature control in this test. The C_d profiles in Figure 7 show similar behaviour for 60 – 138 °C (where Re_t varied from 44 – 104). The same mass flow rate was used in each case, namely 0.40 g s^{-1}, and Re_t increased with temperature owing to the reduction in the oil viscosity. This is consistent with the flow no longer being in the creeping regime: at these temperatures Re_t was over 40. The C_d^{∞} values of 0.6 - 0.7 are similar to those reported in other studies with this nozzle shape (*e.g*. Gu *et al*., 2009). A large difference in C_d values with h/d_t is desirable for gauging, as the associated change in pressure drop across the nozzle is larger. These results suggest that a criterion for selecting the minimum flow rate is that $Re_t > 20$.

The calibration plot obtained for operation at 138 °C and 10 bara in Figure 10 represents proof-of-concept for the high pressure and temperature FDG device. The incremental zone (region B) useful for measuring deposit thickness can be seen for $0.1 < h/d_t < 0.25$. There were noticeable leaks in this test, indicating that some aspects of the hardware require attention in order for the device to operate reliably at 30 bara and 300 °C.

4. 4 Comparison with CFD simulations

Figure 11 compares an experimental calibration plot with the $C_d - h/d_t$ profile generated by the CFD simulations. The inputs to the simulation are the mass flow rate and h/d_t value: ΔP_{12} is extracted from the solution and C_d calculated. The agreement is good and lies within the estimates of experimental uncertainty. Similarly good agreement was obtained at other Re_t values (data not reported). CFD data are not reported for small clearances ($h/d_t < 0.05$) as a very fine mesh was required for these cases and the computer used did not have sufficient memory available. With greater computing resource the curvature region could be identified directly.

Examples of flow velocity distributions generated by the CFD simulation are presented in Figure 12. The maximum *y*-direction velocity is found at the nozzle throat. Flow symmetry is observed for nozzle clearances, in agreement with earlier quasi-static FDG simulations (Gu *et al.*, 2009). Figures 13(*a*) and (*b*) compare the predicted streamlines for Re_t = 11 and 104, respectively. For the former, the flow is

symmetric along the nozzle. At higher Re_t, there is asymmetry near the nozzle and a flow recirculation regime is observed inside the nozzle throat. This may explain the difference in $C_d - h/d_t$ profiles at high Re_t (> 40) and low Re_t (< 20) in Figure 7. At the higher Re_t values, the presence of recirculation regions will lead to an increase in ΔP_{12} and thus larger C_d values.

Figure 14 shows the shear stress, τ_{yr}, exerted on the surface of the inner rod, taken from the CFD simulations. The values plotted are those along the crest of the rod, *i.e*. where the plane of symmetry cuts the cylinder. The shear stress distribution is symmetric in this plane. Large values of τ_{yr} are found under the nozzle lip, where the gap is smallest, and decays to zero at large r. The peak value of approximately 1000 Pa is much larger than that expected for a steady turbulent liquid flow. The latter can be estimated using $\tau \approx C_f \rho U^2/2$: for a typical Fanning friction factor value of $C_f \sim 0.005$, with $\rho \sim 1000$ kg m^{-3} and bulk velocity $U \sim 2$ m s^{-1} gives $\tau \sim 10$ Pa. The large value in this case arises from the high viscosity of the oil at 21 °C and will decrease significantly with temperature.

Also shown on the Figure are values obtained for a laminar flow between parallel discs, reported by Middleman (1998):

$$\tau_{yr} = \left(\frac{3\mu\dot{m}}{\pi\rho h^2}\right)\frac{1}{r} \qquad (9)$$

This result gives good agreement with the CFD simulations in the region beneath the nozzle rim and can therefore be used to estimate the maximum shear stress imposed on the surface.

The shear stress on the inner cylinder surface decreases at locations further from the plane of symmetry as the geometry of a flat nozzle normal to a curved surface means that the gap increases as one moves further from the plane of symmetry. This was demonstrated by Gu *et al.* (2009, 2011b) and was confirmed by the CFD simulations conducted for this work. Equation (9) therefore yields a working estimate of the largest shear stress imposed on the inner rod surface, for consideration when dealing with deformable deposit layers.

Conclusions

A fluid dynamic gauging device has been developed for measuring the thickness of soft fouling layers forming on the inner rod of an annular flow cell at elevated pressure and temperature. Pressure mode FDG operation has been shown to offer several advantages for this duty, including (*i*) fixed gauging flow rate, (*ii*) insensitivity to operating pressure, and (*iii*) large pressure drops as the gauging nozzle approaches the surface which can be exploited for a proximity alarm. Limitations with the hardware on the prototype limited the test range to an upper temperature of 138 ºC and 10 bara.

The results presented here serve as proof of concept. The calibration plots exhibited the features reported in geometrically similar systems using water at ambient conditions by Gu and co-workers. The accuracy of the device is determined by the sensors and by the gauging flow rate. A useful range of discharge coefficient values (and pressure drops) is obtained by setting the flow rate so that $Re_t > 40$. CFD simulations confirmed that the narrow range of C_d values obtained at lower Re_t is due to the transition to a streamline flow pattern in the nozzle throat. This information allows the selection of sensors and operating parameters for a given level of accuracy to be optimised.

CFD simulations showed good agreement with experimental results for the examples considered. The shear stress distribution on the inner annulus surface showed good agreement with the analytical solution for flow between parallel discs and earlier CFD studies on fluid dynamic gauging. The maximum shear stress imposed on the surface being gauged can thus be estimated with reasonable accuracy.

Acknowledgements

A PhD studentship for Tong Gu and equipment funding from the EPSRC (Project EP/D50306X), as well as an RAEng/EPSRC Research Fellowship for Dr John Chew, are gratefully acknowledged. Advice and assistance with the design, construction and instrumentation of the high pressure FDG probe from Andy Hubbard, Surinder Sall and Wei-Yao Ma are also gratefully acknowledged, as are discussions with our collaborators at Imperial College London on the HIPOR fouling test rig.

References

Chew, J.Y.M., Cardoso, S.S.S., Paterson, W.R. and Wilson, D.I. (2004a) CFD studies of dynamic gauging, *Chem Eng Sci*, **59** (16), 3381- 3398.

Chew, J.Y.M., Paterson, W.R. and Wilson, D.I. (2004b) Fluid dynamic gauging for measure the strength of soft deposits, *J Food Eng*, **65**, 2, 175 – 187.

Gordon, P.W., Brooker, A.D., Chew, Y.M.J., Wilson, D.I. and York, D.W. (2010) A scanning fluid dynamic gauging technique for probing surface layers, *Measurement Sci. Tech.*, **21**, 085103.

Gu T., Albert F., Augustin W., Chew Y.M.J., Paterson W.R., Scholl S., Sheikh I., Wang K. and Wilson, D.I. (2011a) Fluid dynamic gauging applied to annular test apparatuses for fouling and cleaning, *Heat Transfer Engineering*, **32**(3-4), 342-351.

Gu, T., Albert, F., Augustin, W., Chew, Y.M.J., Mayer, M., Paterson, W.R., Scholl, S., Sheikh, I., Wang, K. and Wilson, D.I. (2011b) Application of fluid dynamic gauging to annular test apparatuses for studying fouling and cleaning, *Exptl. Thermal Fluid Sci*., **35**, 509-520.

Gu, T., Chew, J.M.J., Paterson, W.R. and Wilson, D.I**.** (2009) Experimental and CFD studies of fluid dynamic gauging in annular flows, *AIChEJ*, **55**(8), 1937-1947.

Jones, S.A., Bird, M.R., Chew, Y.M.J. and Wilson, D.I. (2012) Fluid dynamic gauging of microfiltration membranes fouled with sugar beet molasses, *J. Food Eng*, **108**, 22-29.

Lewis, W.J.T., Chew, Y.M.J. and Bird, M.R. (2012) The application of fluid dynamic gauging in characterising cake deposition during cross-flow microfiltration of a yeast suspension, *J. Membrane Sci*, **405-406**, 113 – 122.

Lister, V.Y., Lucas, C., Gordon, P.W., Chew, J.Y.M. and Wilson, D.I. (2010) Pressure mode fluid dynamic gauging for studying cake build-up in cross-flow microfiltration, *J. Membrane Sci*., **366**, 304-313.

Macchietto S., Hewitt G.F., Coletti F., Crittenden B.D., Dugwell D.R., Galindo A., Jackson G., Kandiyoti R., Kazarian S.G., Luckham P.F., Matar O.K., M. Millan-Agorio O.K., Müller E.A., Paterson W.R., Pugh S.J., Richardson S.M. and Wilson, D.I. (2010) Fouling in crude oil preheat trains: a systematic solution to an old problem, *Heat Transfer Engineering*, **32**(3), 197-215.

Middleman, S. (1998) *An Introduction to Fluid Dynamics: Principles of Analysis and Design*, Academic Press, New York, USA.

Tuladhar, T.R, Paterson, W.R., Macleod, N. and Wilson, D.I. (2000) Development of a novel non-contact proximity gauge for thickness measurements of soft deposits and its application in fouling studies. *Can J Chem Eng*, **78** (5), 935 -947.

Tuladhar, T.R., Paterson, W.R. and Wilson, D.I. (2003) Dynamic gauging in duct flows. *Can J Chem Eng*, **81** (2). 279-284. ISSN 0008-4034.

Appendix

Derivation of $C_d = f\left(\sqrt{Re_t}\right)$

Bernoulli's equation, for an incompressible flow, along a streamline through the gauging nozzle from station 1 to station 2 in Figure 1, is

$$\frac{P_1}{\rho} + \frac{v_1^2}{2} + \rho g h_1 = \frac{P_2}{\rho} + \frac{v_2^2}{2} + \rho g h_2 + f\frac{L}{d_t}\frac{\bar{v}^2}{2} \quad \text{(A.1)}$$

where g is the acceleration due to gravity, L_{eff} is an effective length between stations 1 and 2, f is a friction factor, P_i is the pressure at station i, v_i is the velocity at station i, h_i is the elevation at station I and $\bar{v}$ is the average velocity between stations 1 and 2. The elevation at station 1 and 2 are assumed constant such that:

$$h_1 = h_2 \quad \text{(A.2)}$$

The bulk liquid is effectively stagnant, whilst there are larger velocity at the nozzle throat, such that:

$$v_1 = v_2 \approx 0 \ll \bar{v} \quad \text{(A.3)}$$

For fully developed laminar flow:

$$f = \frac{16}{Re_t} \quad \text{(A.4)}$$

Combining equations (A.1) – (A.4) gives

$$\bar{v} = \sqrt{\frac{\Delta P_{12}}{64}\frac{d_t}{L}Re_t} \quad \text{(A.5)}$$

Where $\Delta P_{12} = P_1 - P_2$

Rearranging equations 3, such that:

$$C_d = \frac{\rho\bar{v}}{\sqrt{2\rho\Delta P_{12}}} \quad \text{(A.6)}$$

and combining with equation (A.5)

$$C_d = \sqrt{\frac{Re_t}{128}\frac{d_t}{L}} \quad \text{(A.7)}$$

i.e.

$$C_d \propto \sqrt{Re_t} \quad \text{(A.8)}$$

Tables

Table 1. Effect of mesh refinement on solution accuracy. Experiment conditions $h/d_t = 0.25$, $Re_t = 11$.

N_e	$C_{d,sim}$	$C_{d,exp}$	% difference	Solution time (s)
13 570	0.113	0.172 (±0.02)	34.3	12
34 442	0.152		13.4	99
55 671	0.168		2.3	205
83 191	0.169		1.9	307

Table 2. Effect of L' on C_d and N_e in simulations for base case in Table 1.

L' (m)	$C_{d,sim}$	$C_{d,exp}$	% difference	N_e
0.22	0.171	0.172	0.87	89 140
0.1775	0.172		0.44	80 954
0.135	0.171		0.81	73 001
0.0925	0.171		0.77	64 401
0.05	0.171		0.86	56 056

Table 3. Comparison of experimental parameters and optimised simulation parameters

Parameter	Apparatus Dimension	Simulation value
l' [m]	0.10 m	0.05 m
L' [m]	0.22 m	0.05 m
□	1	0.125

Figures

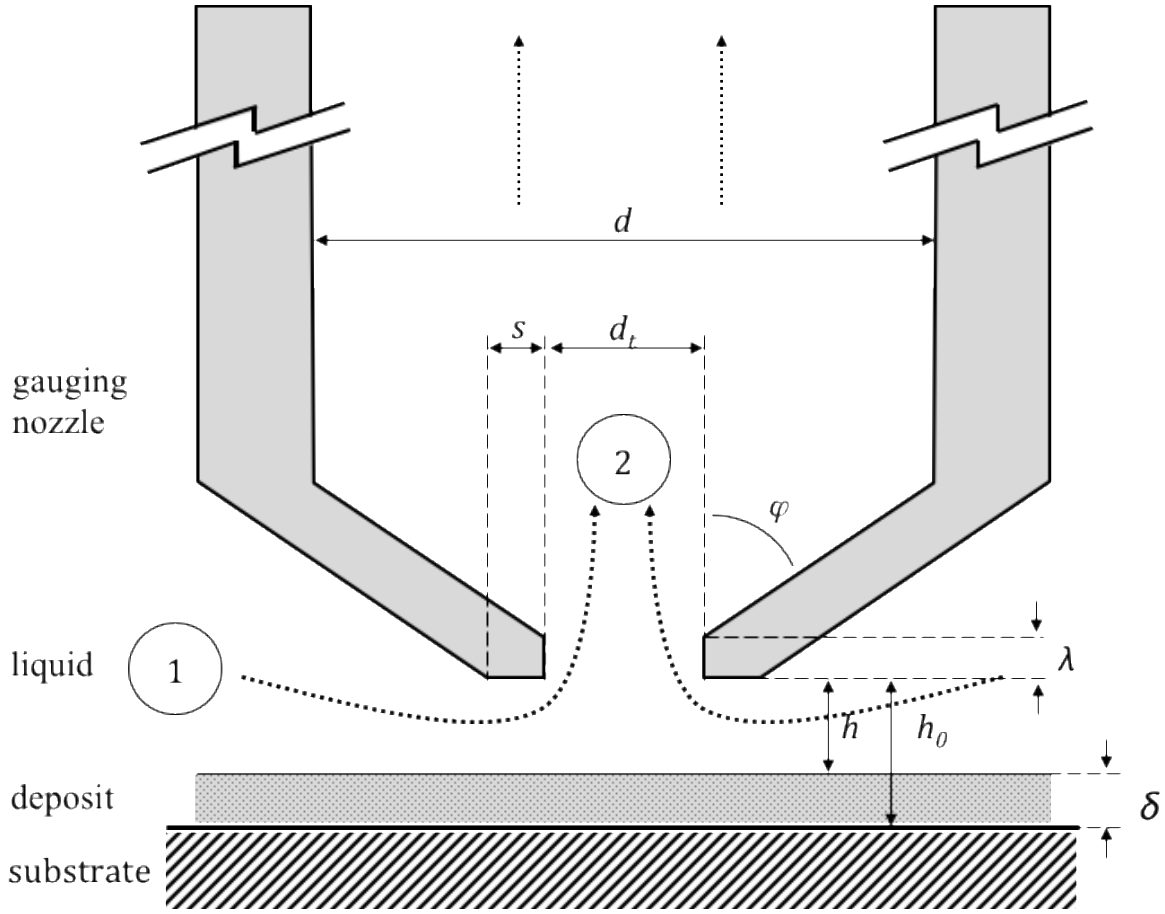

Figure 1. Schematic of an FDG gauging nozzle (not to scale). Dotted lines denote liquid flow path. Stations (1) and (2) indicate the region over which the majority of the pressure drop across the nozzle is generated. Symbols: δ - thickness of deposit layer; h - clearance between nozzle and deposit layer, h_o - clearance between gauging nozzle and substrate surface; d_t - inner diameter of nozzle ; s - lip width; φ- nozzle angle; d - inner tube diameter; λ – nozzle entry length.

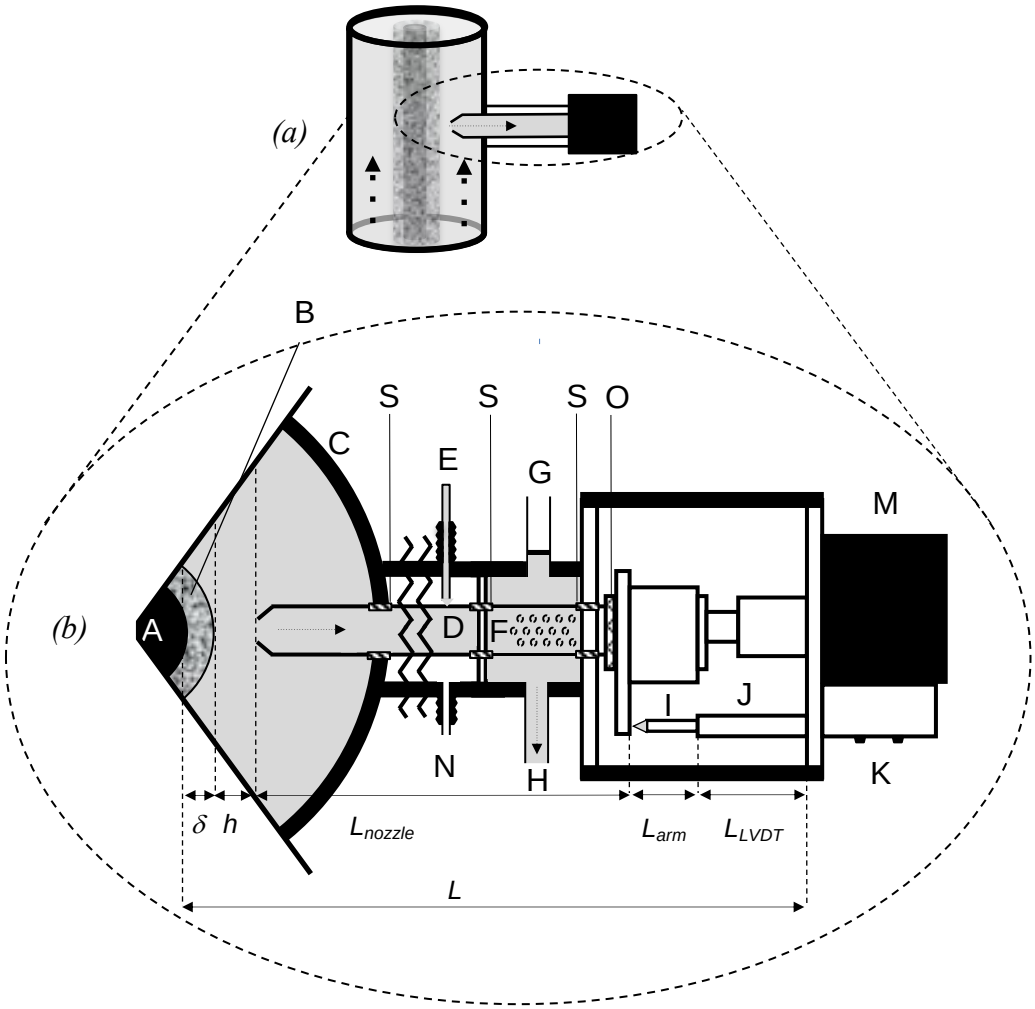

Figure 2. Schematic of the high pressure FDG probe. (a) probe located on annular test section; (b) probe internals. Shading indicates where liquid flows through HIPOR FDG; dashed arrow indicates direction of gauging flow. A - inner annulus wall; B - fouling layer of thickness δ (the tests reported here employed a clean wall); C - outer annulus wall; D - gauging nozzle and tube; E - K-type thermocouple and nitrogen purge; F - section with perforated tube wall; G - port to high point vent; H - gauging liquid exit stream; I - LVDT armature; J - LVDT; K - clamps holding LVDT in fixed position; M - stepper motor; N- nitrogen purge; O – stopper; S - seals. Thickened lines indicate outer walls of the test cell. The gauging nozzle, D, can be completely withdrawn from the annular test section.

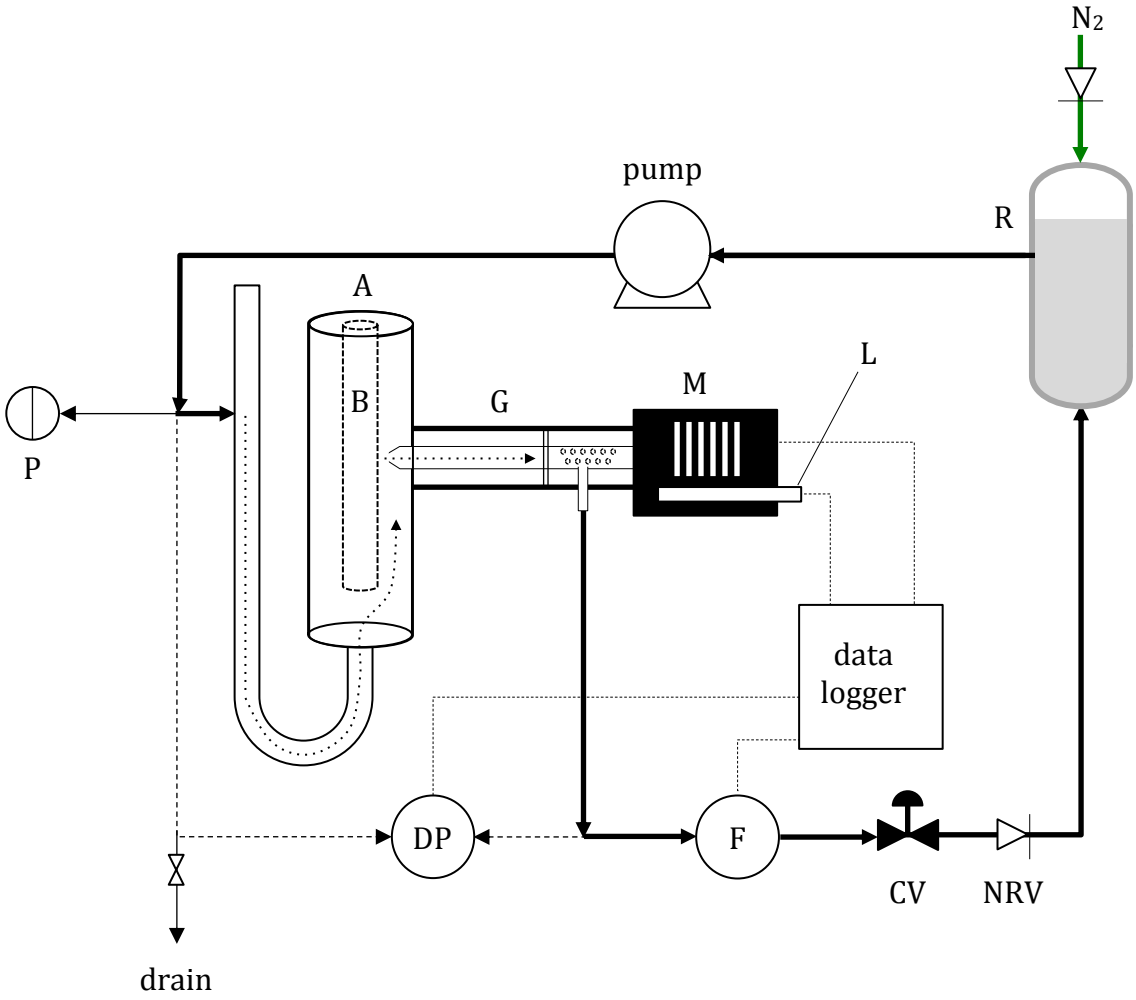

Figure 3. Schematic of the HIPOR FDG test system. Thick lines denote bulk liquid flow path. A – annular test section; B – inner rod; CV – control valve; DP – differential pressure transducer; F – flow meter; G – gauging nozzle and casing; L – LVDT; M – stepper motor; NRV – non return valve; P – pressure indicator; PC – computer; R – liquid reservoir

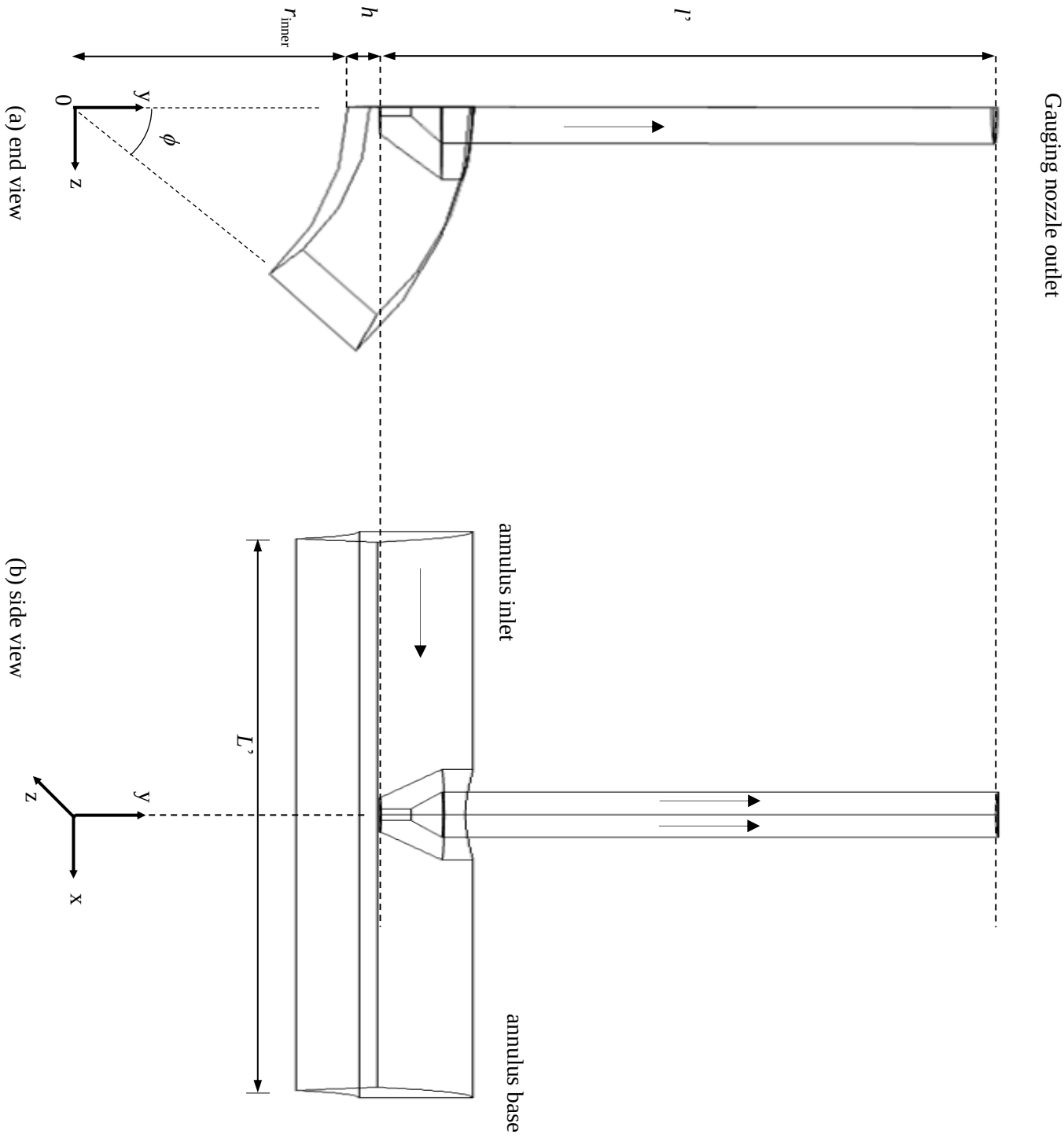

Figure 4. Simulation geometry. The arrows indicate the entry flow in the annulus and exit flow at the tube outlet. Co-ordinates: z- vertical (annulus) axis; y - horizontal (gauging tube) axis. Velocity components *w* and *v* are indicated.

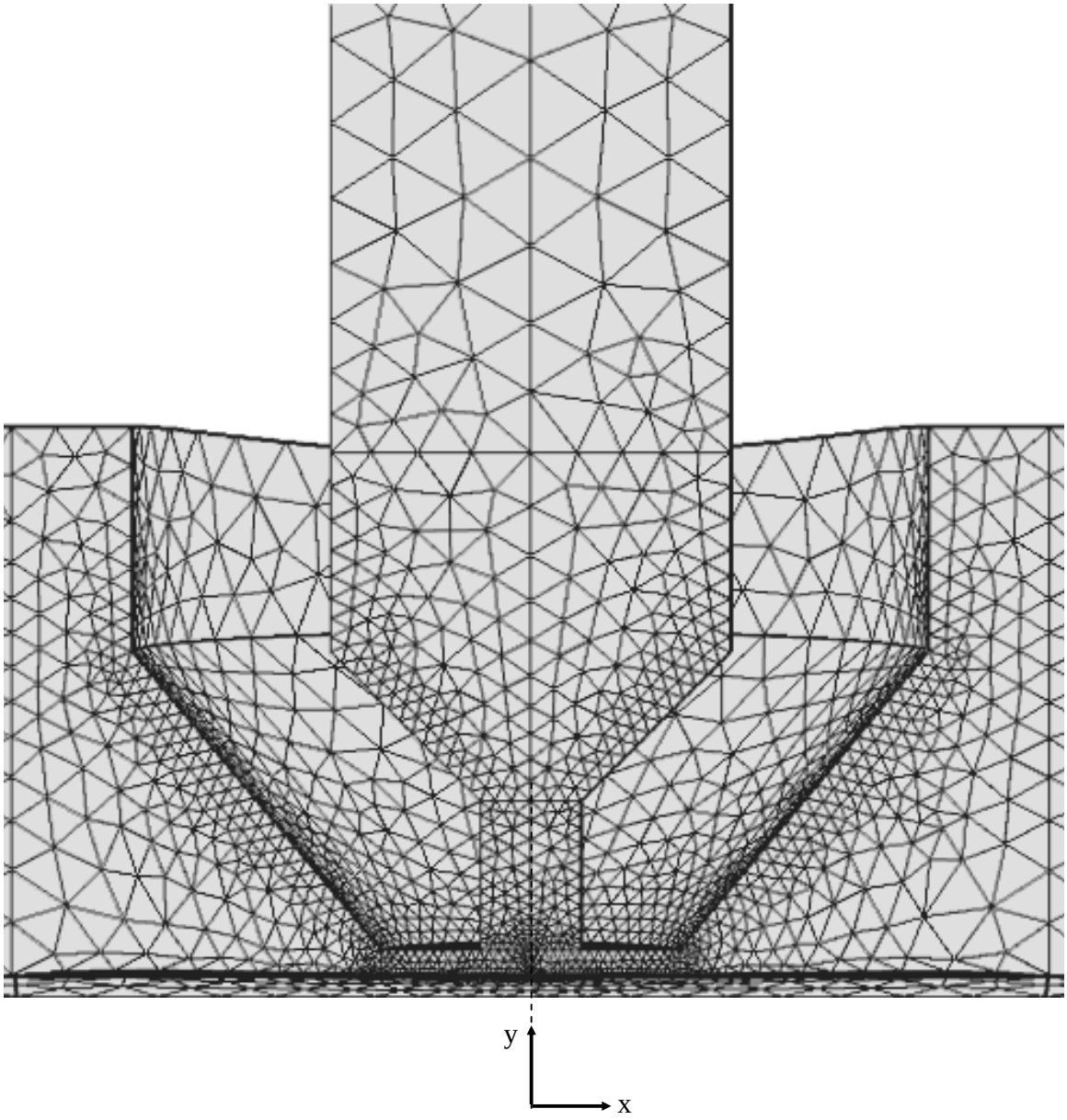

Figure 5. Projection of the mesh in the nozzle region for $h/d_t = 0.25$.

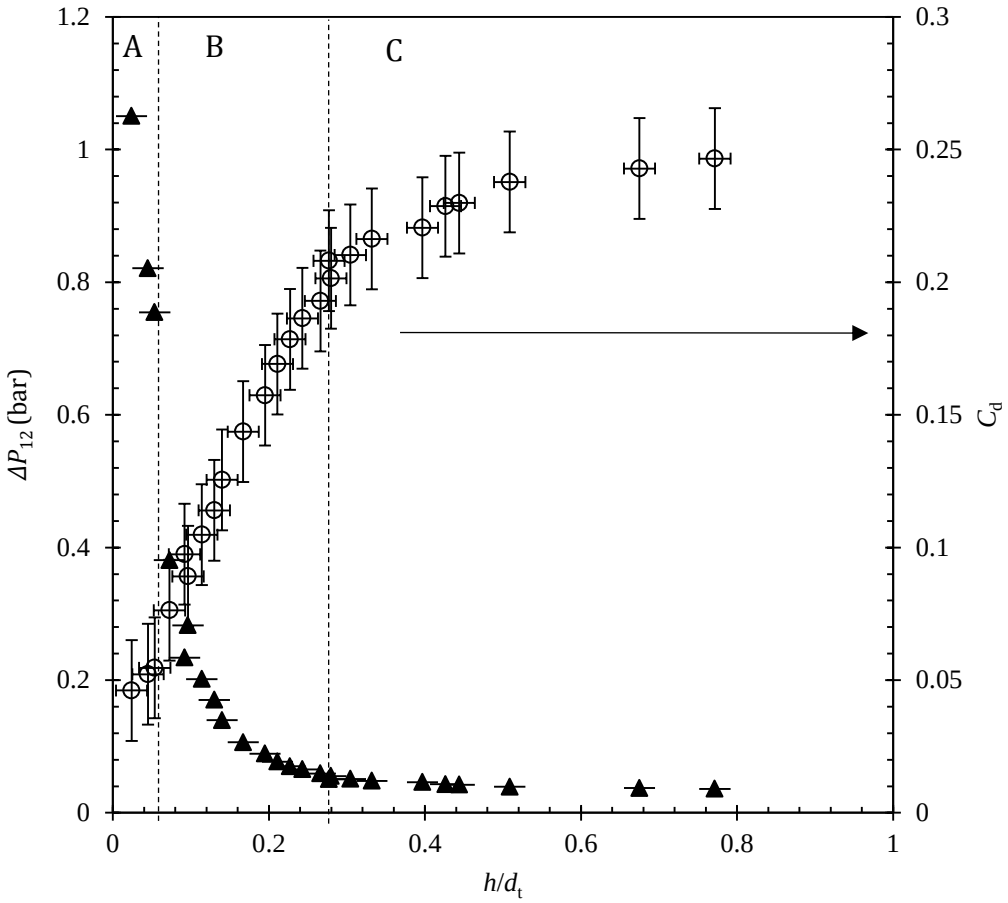

Figure 6. Effect of clearance on pressure drop across nozzle and the corresponding discharge coefficient. Conditions: P = 1 bara, T = 19 °C, $\dot{m}$ = 0.5 g s^{-1}, Re_t ~ 15. Vertical dashed lines separate the regions A, B and C. Solid symbols – ΔP_{12}; open symbols – C_d.

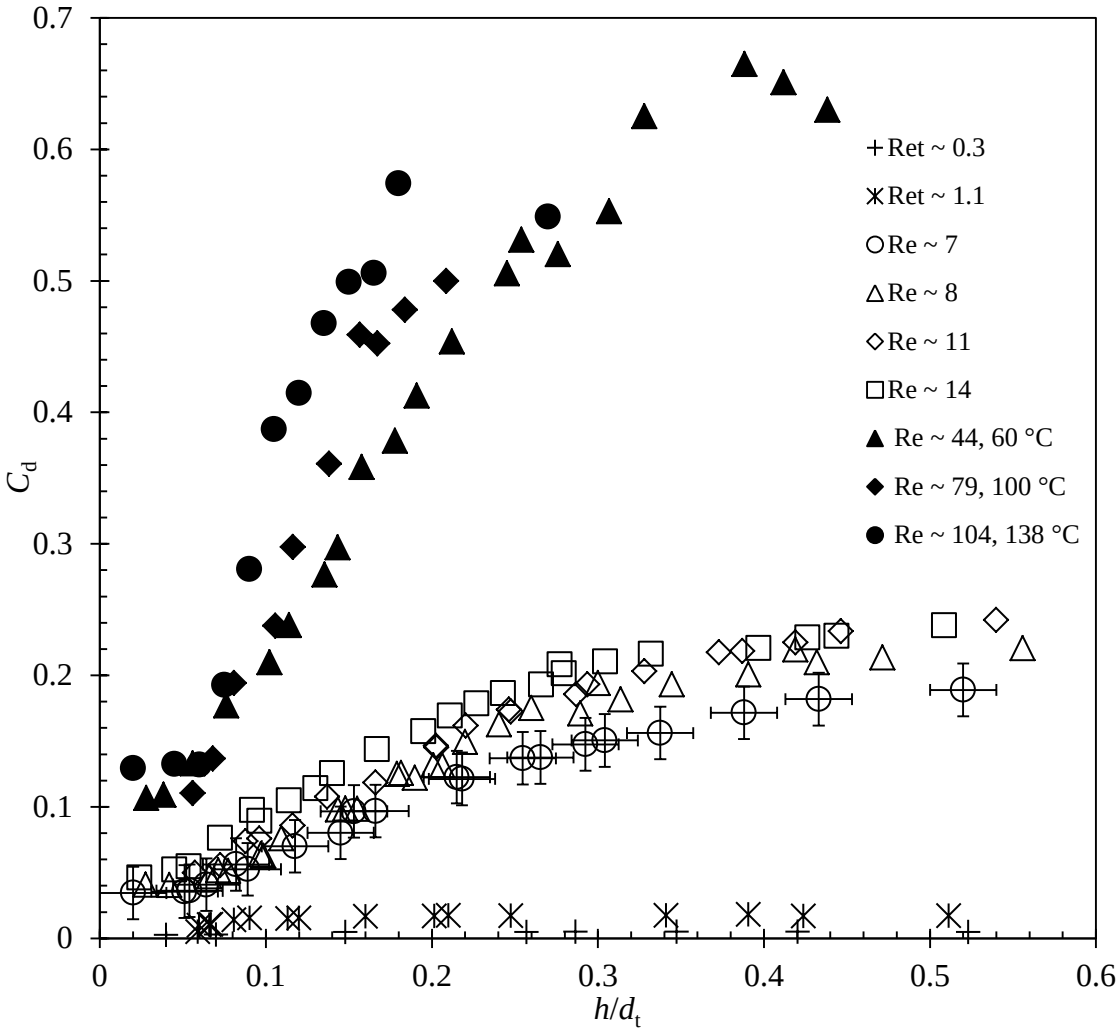

Figure 7. Effect of gauging flow rate on calibration plot profiles. Conditions: 1 bara. Error bars marked on Re_t ~ 7 data set. Open symbols – 19 ºC; Solid symbols - elevated temperature, given in legend.

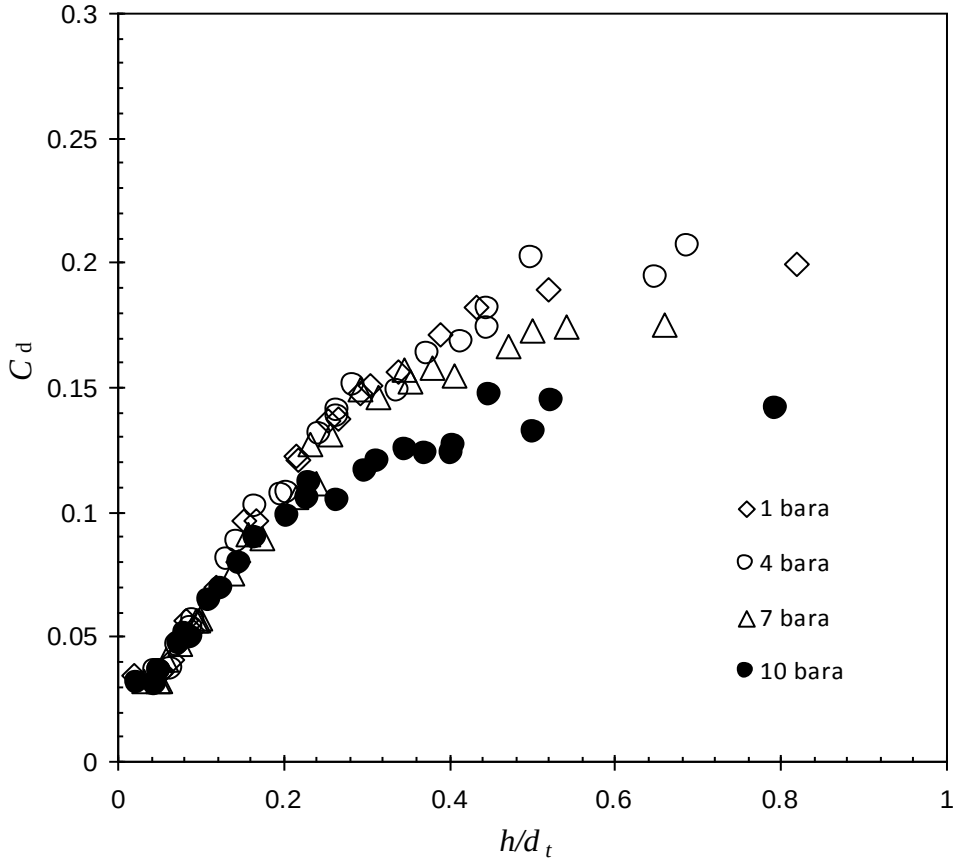

Figure 8. Effect of absolute pressure on $C_d - h/d_t$ profile. Conditions: T = 19 °C, $Re_t \sim 7$.

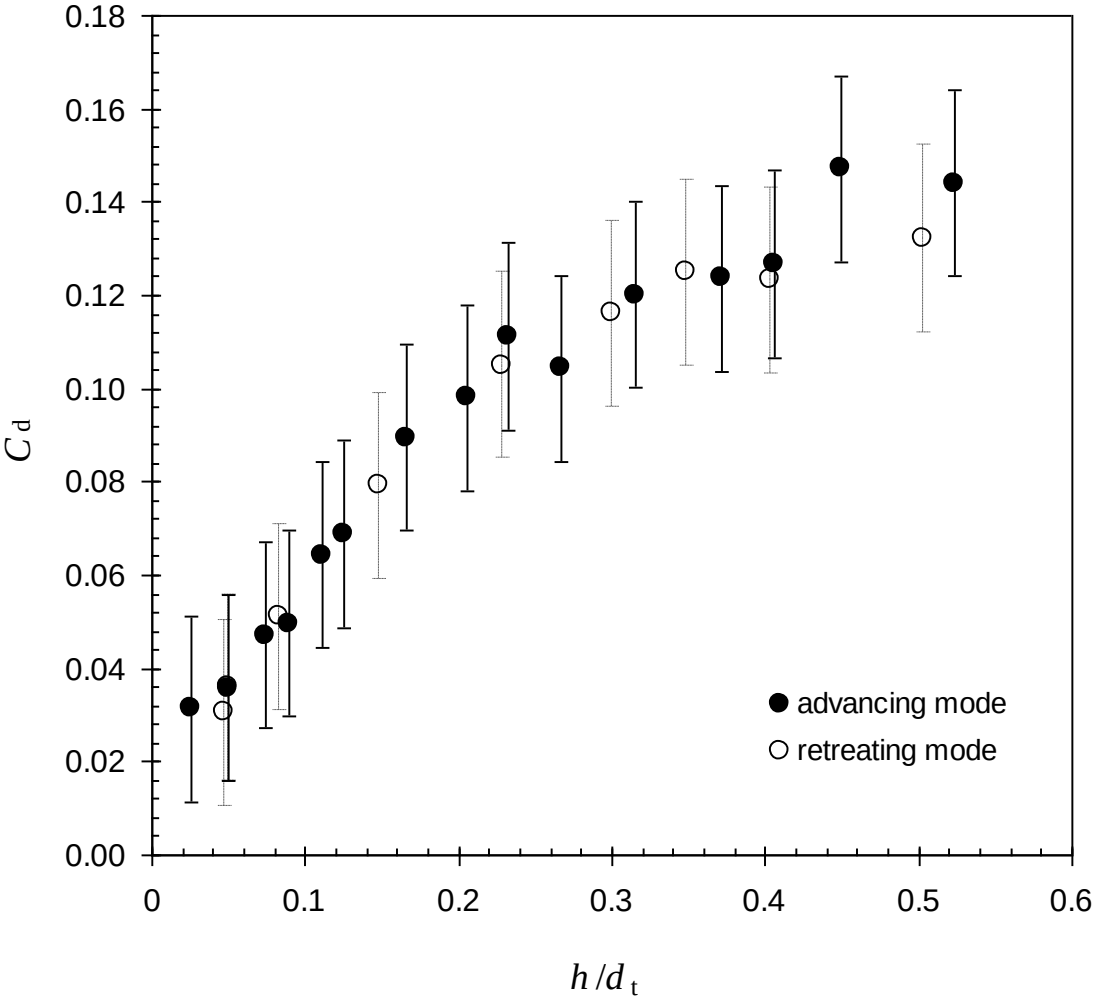

Figure 9. Effect of nozzle clearance on C_d. Conditions: T = 19 °C, P = 10 bara. Solid symbols - advancing mode, open symbols - retreating mode.

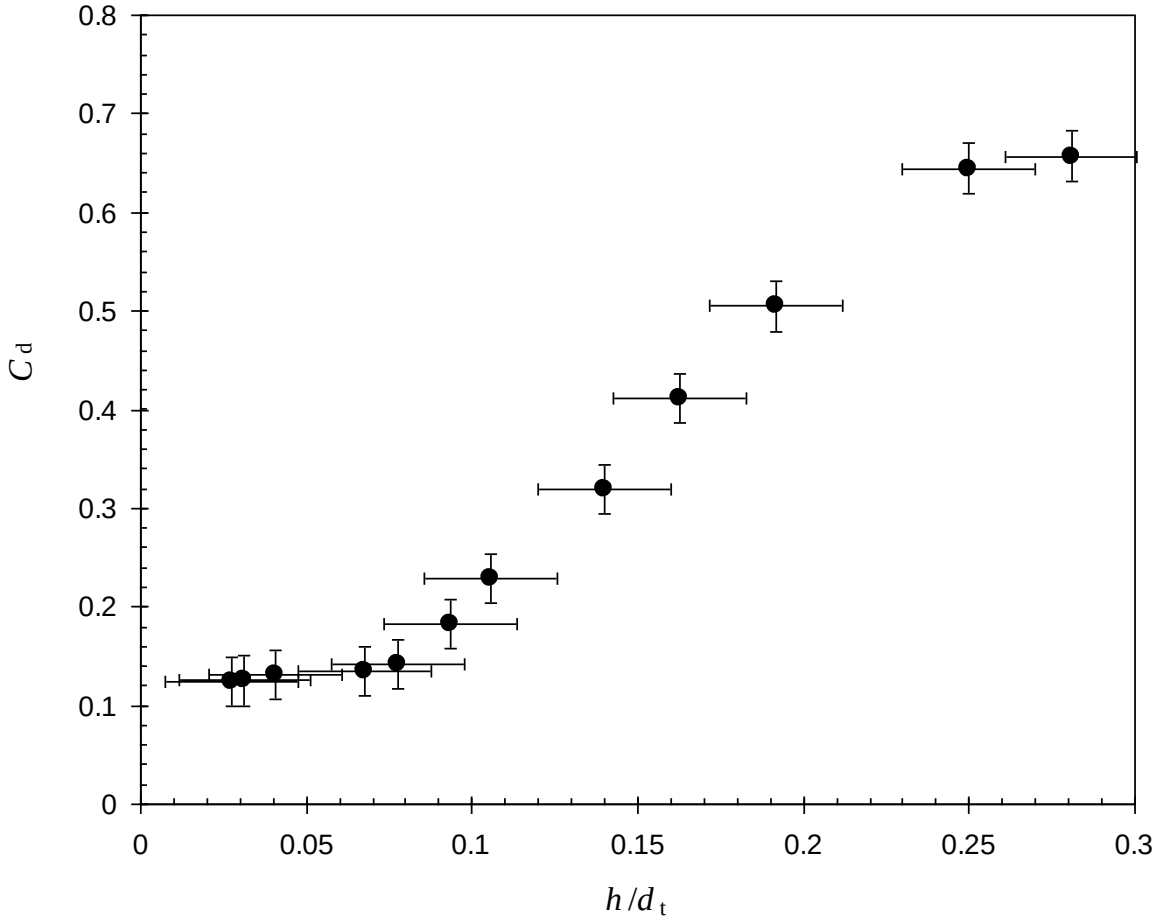

Figure 10. Calibration plot obtained at 10 bara and 138 °C. Gauging flow rate 0.8 g s^{-1}, corresponding to Re_t = 205. Error bars represent measurement uncertainty.

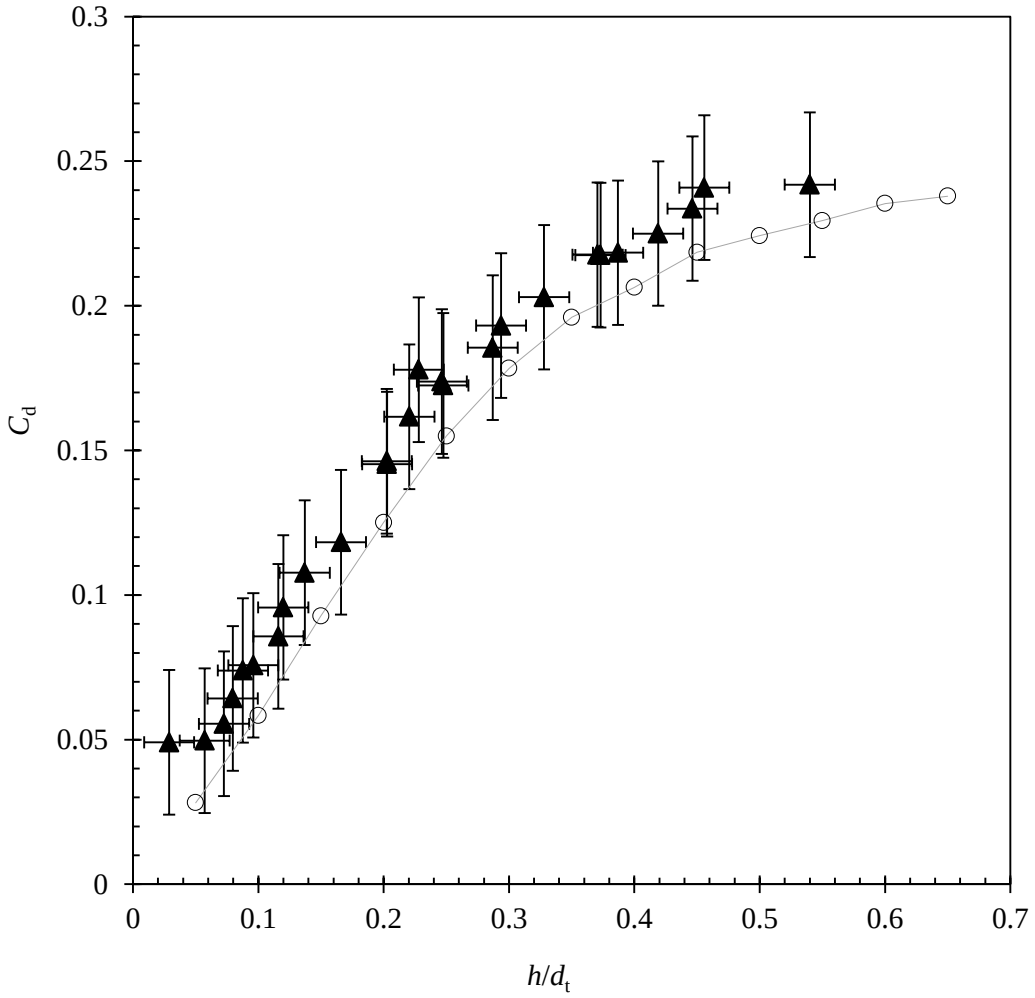

Figure 11. Comparison of experimental C_d profile with values generated by CFD simulation. Conditions: Re_t ~ 11, T = 21 °C. Solid symbols - experimental data; open symbols and dashed interpolation line – simulation results.

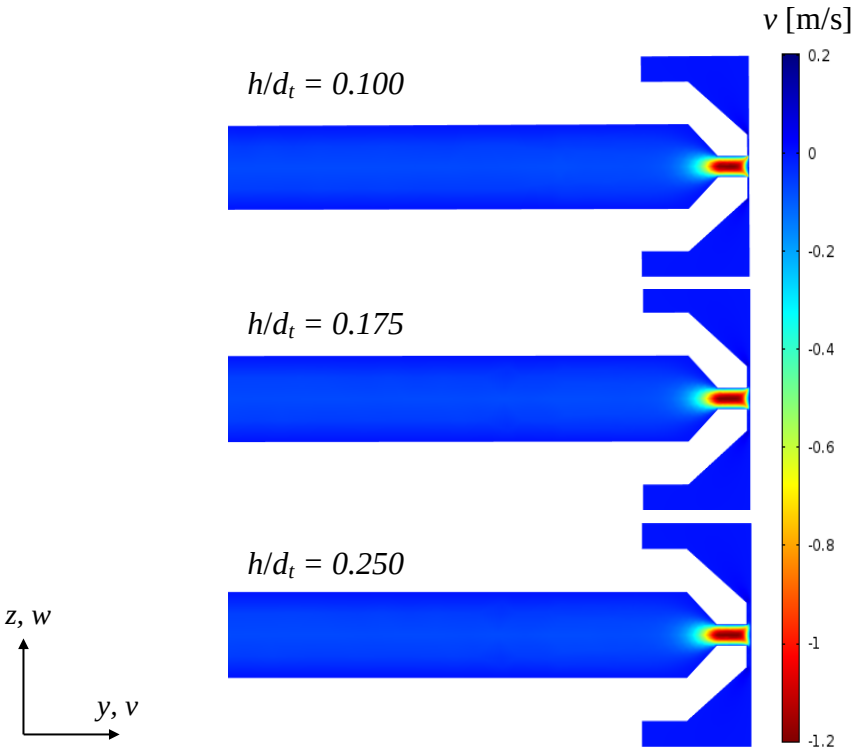

Figure 12. Simulated tube *y*-wise velocity at the *y*-*z* plane of symmetry at Re_t = 11. The simulation shows the maximum *y*-wise velocity occurs at the nozzle throat.

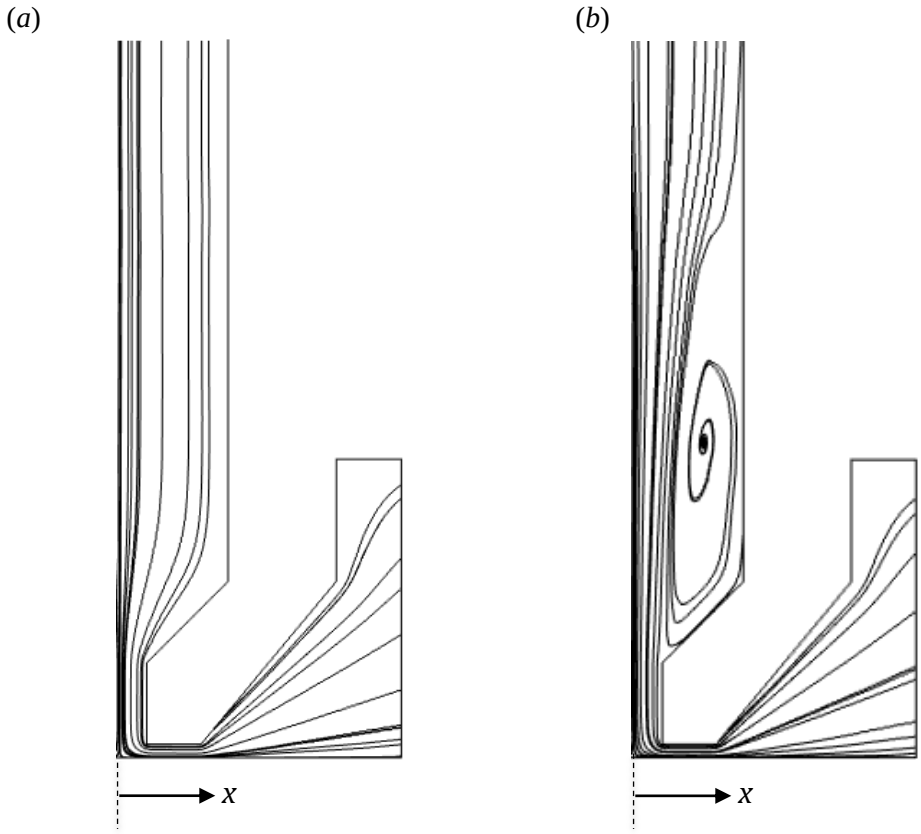

Figure 13. Streamlines obtained from CFD simulations with $h/d_t = 0.25$: (*a*) $Re_t = 11$. (*b*) $Re_t = 104$.

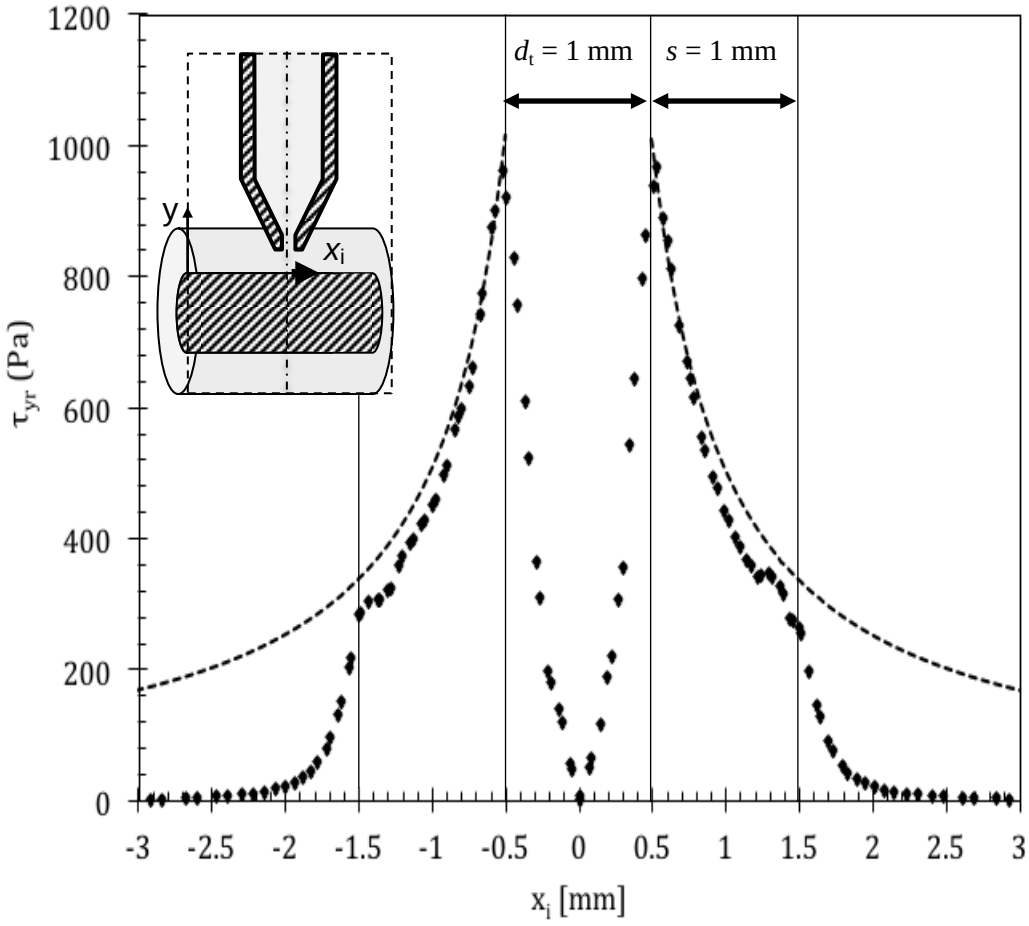

Figure 14. Calculated shear stress imposed by the gauging flow on the crest of the inner annulus surface, as shown in the inset. $x_i = 0$ denotes the gauging tube and nozzle axis. Conditions: $Re_t = 11$, $T = 21$ ˚C, $h/d_t = 0.20$. Vertical lines indicate location of the inner and outer lip of the gauging nozzle. Symbols – data extracted from CFD simulations. Dashed line – Equation (9).